Solar radiation attenuation in a hillside jack pine forest

D. W. A. WHITFIELD[1] AND L. A. MEHLENBACHER[2]
Department of Botany, University of Alberta, Edmonton, Alta., Canada T6G 2E9
AND
C. LABINE
Department of Geography, University of Alberta, Edmonton, Alta., Canada T6G 2E9
Received May 9, 1980

WHITFIELD, D. W. A., L. A. MEHLENBACHER, and C. LABINE. 1982. Solar radiation attenuation in a hillside jack pine forest. Can. J. Bot. **60**: 1913–1922.

A modelling technique for penetration of solar radiation into clumped vegetation canopies is described. It combines Monte-Carlo simulation to determine ray pathlengths through individual plant canopy envelopes with exponential attenuation along these rays. The technique is applied to a hillside forest of randomly located and sized jack pine trees. Scattering effects are incorporated and the model output is compared with field measurements. The results depend on the shape of the tree outline. Attenuation is less rapid with downward cumulative leaf area index than in a randomly dispersed canopy.

WHITFIELD, D. W. A., L. A. MEHLENBACHER et C. LABINE. 1982. Solar radiation attenuation in a hillside jack pine forest. Can. J. Bot. **60**: 1913–1922.

Les auteurs décrivent une méthode de modéliser la pénétration de la radiation solaire à travers une voûte de végétation. Cette méthode combine une simulation de Monte-Carlo pour déterminer la longueur des rayons à travers la voûte de plantes individuelles, avec une atténuation exponentielle le long de ces rayons. La méthode est appliquée à une forêt de pins gris située sur le versant d'une colline et composée d'arbres dont la dimension et la position sont aléatoires. Les effets de diffusion sont incorporés et les prédictions du modèle sont comparées aux mesures prises sur le terrain. Lorsque l'indice de surface foliaire est cumulatif du haut vers le bas, l'atténuation est moins rapide que dans une voûte de feuilles réparties au hasard.

[Traduit par le journal]

Introduction

When the radiation-intercepting elements (leaves, branches) of a plant canopy have a uniform random distribution horizontally, a ray has a probability of penetrating to some depth without interception given by

[1] $$P = e^{-F_c}$$

where F_c is the silhouette leaf and branch area per unit soil area in the layer above the level of interest. This was first established by Monsi and Saeki (1953). For a direct solar beam, P gives the fraction of horizontal area, at the level of interest, which is illuminated by the sun. When sky or diffuse radiation is being considered, Eq. 1 is used to compute radiation penetration separately from different directions, and the result is appropriately averaged to yield overall diffuse penetration. The computation of F_c is often complex, depending on element area, number, shape and orientation, and direction of the ray. Most of the theoretical literature on solar radiation penetration, reviewed by Norman (1975), deals with this problem. Mann *et al.* (1977) treated the effects which occur at a canopy edge and also generalized Eq. 1 to account for element distributions which are horizontally random but nonuniform.

Unfortunately, vegetation is rarely so ideally distributed that Eq. 1 can be used simply. Considerable literature is devoted to various methods of accounting for nonrandomness of location, which may take the form of either clumping or regular dispersal. Nilson (1971) pointed out that Eq. 1 is the zero term in a Poisson distribution and extended the scope of radiation models to include positive and negative binomial distributions. These distributions are empirical in that they contain an arbitrary parameter which must be adjusted to make the distribution fit the data. For a Sitka spruce plantation, Norman and Jarvis (1975) considered the clumping of needles into shoots and shoots into whorls using the Poisson distribution.

In the extreme case of isolated plants or hedgerows, the literature is much less. Brown and Pandolfo (1969) analytically computed interception by opaque, regularly spaced, identical, vertical cylindrical shapes. Isolated plants having ellipsoidal outer envelope shapes were treated by Charles-Edwards and Thornley (1973) for a uniform distribution of foliage within the envelope and by Mann *et al.* (1979) for quadratic and truncated

[1]Present address: Hornby Island, B.C., Canada V0R 1Z0.
[2]Present address: British Columbia Systems Corp., 1112 Fort St., Victoria, B.C., Canada.

0008-4026/82/101913-10$01.00/0

normal distributions. Allen (1974) analyzed interception by a hedgerow of rectangular cross section with a quadratic internal element distribution. Tanaka (1968) used a Monte-Carlo computer technique to compute interception by a tobacco plant community and Oikawa and Saeki (1972) used this technique to explore penetration in square-planted communities. This and other techniques for handling nonrandom distributions are reviewed by Monsi *et al.* (1973).

In this paper we deal with direct and diffuse solar radiation penetration into a hillside forest in which the canopy is so open that many trees do not overlap with any neighbours. The trees are randomly located and variable in size. Thus, no use can be made of models which assume regularity. The partial separation of trees makes Norman and Jarvis's (1975) model inapplicable. New techniques were required to produce a model which is free of empirical tuning parameters.

The original motivation for this work was the need for a radiation component of a water and energy balance model which was developed as part of a study of revegetation of areas disturbed by the mining of oil sands. The problems encountered and techniques developed for handling them make this radiation model of interest in itself.

Study site

We worked on a southwest-facing hillside at the Richardson Fire Tower (57°53′N, 110°58′W), about 140 km NNE of Fort McMurray, Alta. The site is forested with an almost monospecific stand of *Pinus banksiana* Lamb., with an understory mainly of lichens and low shrubs. It is in the Athabasca south forest region (Rowe 1972). Carroll and Bliss (1981) describe the vegetation of the region. The hillside stand was even aged, dating from a fire in 1930 or 1931 (44–47 years before this study). No tree species other than *P. banksiana* occurred in the study plots.

Table 1 summarizes site geometry and tree characteristics. The area indices of that table may be combined with the height distributions of element number density (Fig. 1) to yield approximate height distributions of area indices. Measurement methods, including the test for random tree location, are outlined below.

TABLE 1. Site characteristics of the hillside forest

Hill slope (average from horizontal), °	22
Hill aspect (azimuth from true north), °	250
Forest stem density ($dbh > 0.01$ m), m^{-2}	0.66
Average tree height[a], m	4.4
Tree height range, m	1.2–9.7
Cummulative leaf area index[b]	6.1
Cummulative branch area index[b]	0.47
Cummulative trunk area index[b]	0.23
Cummulative seed cone area index[b]	0.25

[a]Measured vertically. The data of Fig. 1 are expressed in a coordinate system perpendicular to the hill slope.
[b]These indices are based on total surface area, not projected area.

Model structure

The problem we treat here is that of the interception and scattering of solar radiation in a hillside forest of isolated, randomly located trees of uniform envelope shape but random size distribution. In view of the geometric complexity, we did not attempt an analytical solution (and in fact suspect that none is possible), but we combined a Monte-Carlo simulation to get within-envelope pathlengths with the application of Eq. 1 along these paths. Scattering was accounted for by a method of Norman and Jarvis (1975). The geometrical and optical characteristics of the trees were derived from measurements on material from the Richardson site, and the model output is compared with transect measurements of radiation attenuation at that site.

The field situation was somewhat idealized in the following gemoetrical assumptions of the model: (*a*) The hillside is a flat plane of slope α_s from the horizontal and azimuth ω_s (azimuthal direction from true north of a normal to the slope). (*b*) The trees are randomly located with their trunks vertical and thus at an angle α_s to a normal to the slopes. (*c*) Tree heights are random, with the empirical distribution shown in Fig. 1. (*d*) Each tree is in the shape of a cylinder capped with a cone. The cylinder radius is linearly related to tree height. (*e*) All vegetational elements (needled shoots, bare live branches, dead branches, and cones) are randomly distributed within the above-tree envelope with a uniform distribution horizontally, and the empirical vertical distributions are shown in Fig. 1.

For comparison, two other geometrics were also considered: (*i*) a horizontally random canopy (no clumping into trees) and (*ii*) a canopy of flat-topped trees having the same height, density, and spacing as the pointed trees.

Computations were performed in a Cartesian coordinate system having z direction perpendicular to the hillside and x direction down the slope. Ray origin direction is given by azimuth, ϕ, clockwise from above from the x-axis and zenith angle, η, from the z-axis.

The only symmetry in the problem is a reflection in a plane perpendicular to the hillside, aligned up and down the slope. Thus, we consider $0 \leq \phi \leq \pi$ and $0 \leq \eta \leq \pi/2$.

Penetration probabilities

The canopy is conceptually divided into layers. For any element type, k, the probability P_i^k of noninterception of a ray from direction η,ϕ to the bottom of layer i is given by a straightforward modification of Eq. 1.

$$[2] \qquad P_i^k(\eta,\phi) = \frac{1}{N_j}\sum_{j=1}^{N_j} e^{-\rho_i^k \bar{A}^k(\eta,\phi) L_i^j(\eta,\phi)}$$

where an average is taken over N_j randomly chosen rays, $L_i^j(\eta,\phi)$ is that part of ray j's path from the canopy top to the bottom of layer i which is contained within tree outline envelopes, $\bar{A}^k(\eta,\phi)$ is the average projected area of an element of type k viewed from η,ϕ, and ρ_i^k is average volume density of element type k within the envelope above layer i. This is equivalent to the approach of Charles-Edwards and Thornley (1973), except for determination of the L's, as will be described below. Equation 2 was applied to all intercepting elements except trunks; these were idealized as vertical cones,

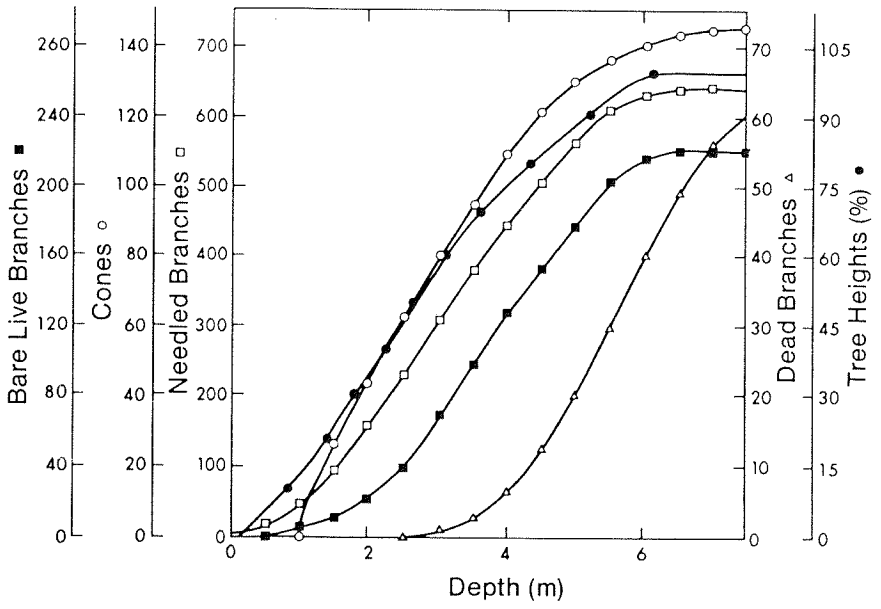

FIG. 1. Distributions of tree heights and element densities with depth in the canopy, accumulated from the top down. Element density is in numbers per tree. Depth is measured perpendicular to the hill.

with the height distribution indicated in Fig. 1. Then

$$[3] \qquad P_i^t(\eta) = e^{-\left(\rho^t \sum_{j=1}^{i} g_j A_j^i(\eta)/\cos\eta\right)}$$

where ρ^t is stand density (0.66 m^{-2}), g_j is the proportion of trunks reaching into layer j, and $A_j^i(\eta)$ is the area, projected onto the plane bottom of layer i, of trunks in height class j. The trunks are assumed for simplicity to be perpendicular to the slope. This crude approximation is acceptable because they contribute little to total interception (Fig. 4).

The probabilities of noninterception by the separate elements are combined into an overall noninterception probability

$$[4] \qquad \hat{P}_i(\eta,\phi) = P_i^n(\eta,\phi)P_i^c(\eta,\phi)P_i^b(\eta,\phi)P_i^d(\eta,\phi)P_i^t(\eta)$$

where P_i^n, P_i^c, P_i^b, P_i^d, and P_i^t refer to noninterception probabilities for needled shoots, cones, bare live branches, dead branches, and trunks, respectively.

From $\hat{P}_i(\eta,\phi)$ we may determine the penetration probability ($\bar{P}$) of sky radiation in the usual way:

$$[5] \qquad \bar{P}_i = \frac{\int_0^{\pi/2} d\eta \int_0^{\pi} d\phi\, \Gamma(\eta,\phi)\hat{P}_i(\eta,\phi)\sin\eta\cos\eta}{\int_0^{\pi/2} d\eta \int_0^{\pi} d\phi\, \Gamma(\eta,\phi)\sin\eta\cos\eta}$$

where $\Gamma(\eta,\phi)$ is the brightness of the sky in the direction η,ϕ. The results presented below were computed with $\Gamma = 1$. Setting $\Gamma = 1$ for the part of the hemisphere (viewed from the hillside coordinate system) occupied by sky and $\Gamma = 0$ for that occupied by flatland forest below the hill makes only a 4% difference near the canopy top and even less difference deeper in the canopy.

Pathlengths

The within-envelope ray pathlengths, $L_i^j(\eta,\phi)$, used in Eq. 2 were computed by a Monte-Carlo technique, which is to say that the interception points of randomly chosen rays with randomly located trees were determined numerically. A "numerical forest" having stem density and tree height distribution corresponding to the field situation was generated by calls to a random number generator. For a given ray origin direction, starting points at the canopy top were chosen randomly and the rays were followed through the canopy to ground level, calculating all interception points with tree envelopes. Preliminary simple calculations determined whether the ray came close to a given tree. If it did, a more complete calculation was performed. This combined the ray path equation with those representing the cylinder and cone of the tree. Each combination was a quadratic in z, the other coordinates having been eliminated. If this quadratic had imaginary roots, no intersection occurred; real roots represented intersection points. For each direction, 500 rays were traced in this fashion, so $N_j = 500$ in Eq. 2. This number was arrived at empirically by examining the convergence of

$$\frac{1}{N_j}\sum_{j=1}^{N_j} L_n^j,$$

where n represents the canopy bottom.

Projected element areas

The needled shoots, live bare branches, and dead branches were all idealized as independently distributed right circular cylinders. Seed cones were treated as spheres of radius 1.47 cm (average from field measurements).

For a cylinder of length l and diameter d, viewed from a direction at an angle α to the cylinder axis, the projected area is

$$[6] \quad A(\alpha) = dl \sin\alpha + \pi\left(\frac{d}{2}\right)^2 \cos\alpha$$

If the viewing direction is η,ϕ and the cylinder axis has an orientation $\hat{\eta},\hat{\phi}$, α is easily calculated from the cosine law of spherical trigonometry:

$$[7] \quad \cos\alpha = \cos\hat{\eta}\cos\eta + \sin\hat{\eta}\sin\eta\cos(\phi - \hat{\phi})$$

For needled shoots, the cylinders are partially transparent because of gaps between the needle projections. We designate the opaque fraction of the projected area $\Omega(\alpha)$. For the distributions of element size, f^k (l,d), and orientation, F^k $(\hat{\eta},\hat{\phi})$, the averaged projected area, for use in Eq. 2, is

$$[8] \quad \bar{A}^k(\eta,\phi) = \frac{\sum_{M_l=1}^{N_l}\sum_{M_d=1}^{N_d}\sum_{M_{\hat{\eta}}=1}^{N_{\hat{\eta}}}\sum_{M_{\hat{\phi}}=1}^{N_{\hat{\phi}}} f^k(l,d)F^k(\hat{\eta},\hat{\phi})A(\alpha)\Omega(\alpha)}{\sum_{M_l=1}^{N_l}\sum_{M_d=1}^{N_d}\sum_{M_{\hat{\eta}}=1}^{N_{\hat{\eta}}}\sum_{M_{\hat{\phi}}=1}^{N_{\hat{\phi}}} f^k(l,d)F^k(\hat{\eta},\hat{\phi})},$$

where l, d, $\hat{\eta}$, and $\hat{\phi}$ are taken at discrete intervals, of which there are N_l, N_d, $N_{\hat{\eta}}$, and $N_{\hat{\phi}}$, respectively. For elements other than needle clumps, $\Omega(\alpha) = 1$.

Scattering

Our scattering calculations follow Norman and Jarvis (1975) with some adaptations and notational changes. Figure 2 illustrates the terminology. E_i and E_i' are the downward and upward diffuse fluxes above layer i, and F_i and F_i' are the contributions of diffuse flux arising within layer i owing to scattering of the intercepted direct solar beam B_i. Then for layer i and layer j immediately below it

$$[9] \quad E_j = \tau_i E_i + \rho_i E_j' + F_i$$

and

$$[10] \quad E_i' = \tau_i E_j' + \rho_i E_i + F_i'$$

where τ_i and ρ_i are the transmissivity and reflectivity, respectively, of layer i, assumed to be the same from below as above. This pair of equations may be written out for each of the n layers. At the ground surface,

$$[11] \quad E_{n+1}' = \rho_g E_{n+1}$$

At this point, the problem is conveniently divided into two parts: the scattering of radiation arriving at the canopy top as diffuse sky radiation and the scattering of intercepted solar beam. In the former case, we set $E_1 = 1$, $F_i = 0$, and $F_i' = 0$ for all i and arrive at $2n + 1$ equations in $2n + 1$ unknowns (E_1', E_2, E_2' ... E_n, E_n', E_{n+1}, E_{n+1}'), which can be solved by the fast algorithm described by Norman and Jarvis (1975). The second case, scattered solar beam, is not so simple. The F_i's and F_i''s must be determined (as described below), and although setting $E_1 = 0$ again yields $2n + 1$ equations in $2n + 1$ unknowns, the fast algorithm is unstable and a Gaussian elimination procedure was used.

If all diffuse radiation is isotropic, we need not account for its angular distribution. In that case, open-space layer transmissivity is simply

$$[12] \quad \tau_i^0 = \frac{\bar{P}_i}{\bar{P}_{i-1}},$$

To this must be added that diffuse radiation which is intercepted and reflected or transmitted. The scattering of diffuse radiation is treated by Norman and Jarvis (1975) in their Appendix A. They show that for randomly oriented scattering elements, all having the same properties, one quarter of reflected radiation is forward scattered and three quarters is backward scattered. Of that transmitted, three quarters is forward and one quarter is backward. Thus,

$$[13] \quad \tau_i = \tau_i^0 + \tfrac{1}{4}[\rho^t\bar{I}_i^t + \rho^c\bar{I}_i^c + \rho^b\bar{I}_i^b + \rho^d\bar{I}_i^d + \rho^n\bar{I}_i^n] + \tfrac{3}{4}\rho\tau^n\bar{I}_i^n$$

and

$$[14] \quad \rho_i = \tfrac{3}{4}(\rho^t\bar{I}_i^t + \rho^c\bar{I}_i^c + \rho^b\bar{I}_i^b + \rho^d\bar{I}_i^d + \rho^n\bar{I}_i^n) + \tfrac{1}{4}\tau^n\bar{I}_i^n$$

where $\bar{I}_i^k$ is the fraction of diffuse radiation incident on layer i which is intercepted by element type k, and ρ^k and τ^k are the reflectivity and transmissivity of element type k, respectively. Then, we designate by $I_i^k(\eta,\phi)$ the fraction of canopy top radiation from η,ϕ which is intercepted by element type k in layer i:

$$[15] \quad I_i^k = \frac{(P_{i-1}^k(\eta,\phi) - P_i^k(\eta,\phi))(\hat{P}_{i-1}(\eta,\phi) - \hat{P}_i(\eta,\phi))}{\sum_k (P_{i-1}(\eta,\phi) - P_i^k(\eta,\phi))}$$

Above the top layer, the P's and $\hat{P}$'s are unity. Then $I_i^k(\eta,\phi)/\hat{P}_{i-1}(\eta,\phi)$ is the fraction of diffuse radiation from η,ϕ incident on the top of level i which is intercepted in level i

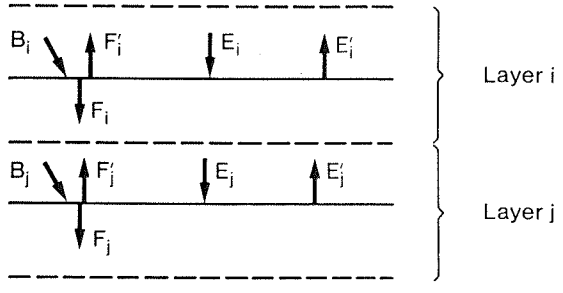

FIG. 2. Symbols used in scattering calculations. The downward (E) and upward (E') diffuse fluxes apply to layer tops, while downward (F) and upward (F') scattered solar beam (B) are considered as originating in the layers.

by element type k, and

$$[16]\quad \bar{I}_i^k = \frac{\int_0^{\pi} d\phi \int_0^{\pi/2} d\eta I_i^k(\eta,\phi)/\hat{P}_{i-1}(\eta,\phi) \sin\eta\cos\eta}{\int_0^{\pi} d\phi \int_0^{\pi/2} d\eta \sin\eta\cos\eta}$$

This completes the calculation of the τ_i's and ρ_i's. To consider the interception of the solar beam, the F_i's and F_i''s must be evaluated. Again we used Appendix A of Norman and Jarvis (1975):

$$[17]\quad R_i = \rho^t\bar{I}_i^t + \rho^c\bar{I}_i^c + \rho^b\bar{I}_i^b + \rho^d\bar{I}_i^d + \rho^n\bar{I}_i^n,$$

$$[18]\quad F_i = (1 - f_w(\eta))R_i + f_w(\eta)\tau^n\bar{I}_i^n,$$

and

$$[19]\quad F_i' = f_w(\eta)R_i + (1 - f_w(\eta))\tau^n\bar{I}_i^n$$

where $f_w(\eta)$ is tabulated by Norman and Jarvis for weighted average scattering. These scattering calculations must be performed separately for each wavelength of interest, as the element optical characteristics are wavelength dependent.

Partitioning of incident radiation and calculation of total fluxes

The radiation components measured as described in the next section permit us to partition the solar radiation fluxes into direct beam and diffuse components. First, the diffuse S_d may be divided between visible (280–695 nm) and near-infrared (695–2850 nm) components:

$$[20]\quad S_d^v = 0.7S_d$$

and

$$[21]\quad S_d^r = 0.3S_d$$

which follows Ross (1975). The beam components then follow from the above and the measured total, S_t, and total near infrared, S_t^r:

$$[22]\quad S_b^r = S_t^r - S_d^r$$

$$[23]\quad S_b^v = S_t - S_d - S_b^r$$

Then, for sun position η,ϕ, we can write down the downward fluxes at the bottom of canopy level i as fractions of their values at the canopy top. For the visible,

$$[24]\quad V_i = [\epsilon(S_b^v(E_i^{bv}(\eta,\phi) + \hat{P}_i(\eta,\phi)) + S_d^vE_i^{dv}) + (1 - \epsilon)(S_b^vE_i'^{bv}(\eta,\phi) + S_d^vE_i'^{dv}(\eta,\phi))]/(S_b^v + S_d^v)$$

where the E's are solutions of Eqs. 9 and 10, the superscripts b and d refer to beam and diffuse components, respectively, and ϵ is the cosine-weighted proportion of the sensor's hemisphere which sees downward scattered radiation. This enters into the calculation because of the angle α between the hillside normal and a normal to the sensor, which is mounted vertically. The value of ϵ for $\alpha = 27°$ is 0.9633. The total downward infrared flux is similarly calculated.

Measurements

Radiation

Our method for the measurement of solar radiation attenuation in the forest canopy was similar to that of Norman and Jarvis (1974). Vertical towers 9 m high were established 20 m apart. At chosen heights, wire pairs 15 cm apart in a horizontal plane were stretched taut between the towers. A teflon-skidded sled, 18 × 18 cm, bearing sensors with their axes vertical, was towed along the wires at a uniform tow speed from tower to tower. A data acquisition system periodically recorded the signals from the sled-mounted sensors and from similar ones atop a tower above the canopy. The readings were made approximately every 2 cm along the transects.

Two different cosine-corrected sensor types were used, both manufactured by Lambda Instruments Corp. Model LI-190S responds nearly equally to photon numbers in the wavelength band 400–700 nm, with nearly zero response outside this band. Model LI-270S responds to a band about 70 nm wide around 780 nm.

In processing the data logger output, the ratios of sled sensor to tower sensor output were computed for each set of readings and averaged along the transects. Two transect stations were used, with four levels at one and three at the other.

Simultaneously with the above, measurements were taken on the hilltop of total solar, diffuse solar, and near-infrared

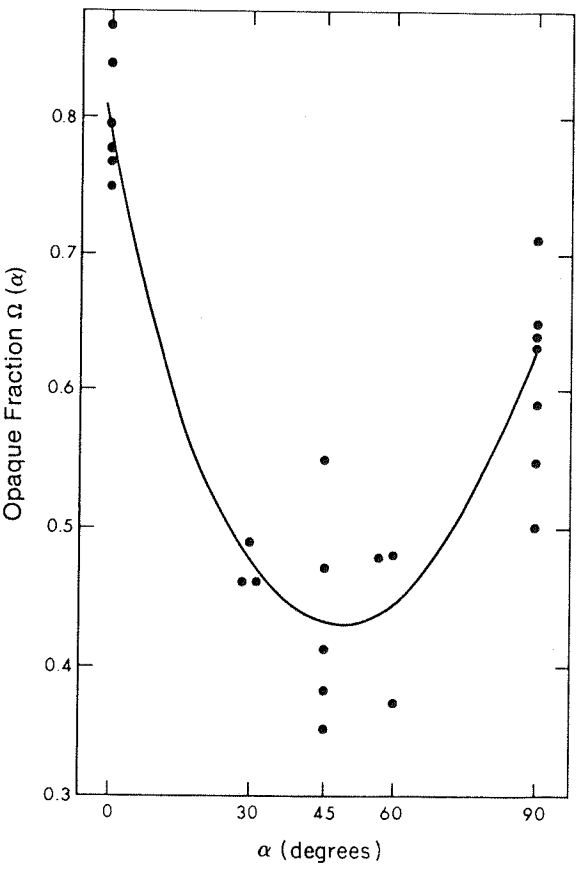

FIG. 3. Fraction of needle clump outline occupied by needles or branch when viewed from various angles from the clump axis. The points are individual measurement results and the curve is that used in model calculations.

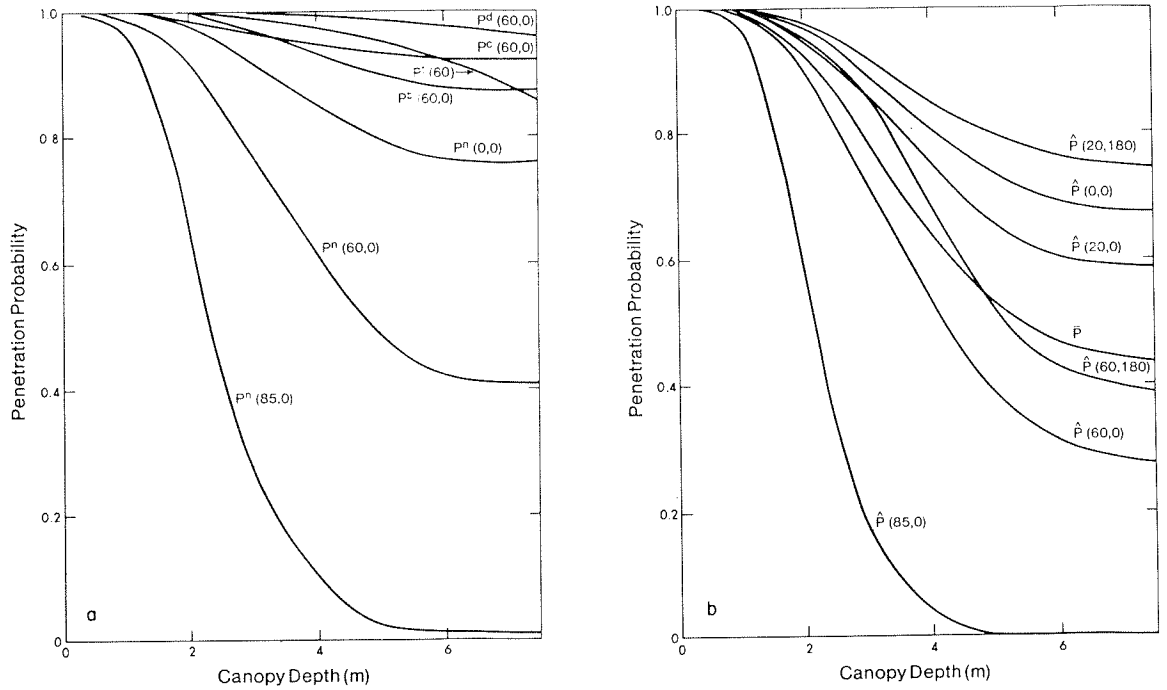

FIG. 4. Typical results from the penetration probability model. (*a*) Probabilities of noninterception by each element type for $\eta = 60°$, and additionally for needle clumps at $\eta = 0$ and 85°, all for $\phi = 0°$. P^n, P^c, P^b, and P^d denote probabilities for needle clumps, cones, live branches, and dead branches, respectively. (*b*) Overall penetration probabilities (P) for a variety of incident directions, and average penetration from a uniformly bright sky ($\bar{P}$).

solar radiation. The sensors were Eppley precision pyranometers, the first and second with transparent glass domes, the second equipped with a shadow band, and the third covered with a Schott glass filter transmitting in the band 695–2850 nm. Readings from the sensors were averaged over half-hour intervals.

Tree spacing and geometry

Randomness of tree placement was tested over a 10 × 20 block by the method of Clark and Evans (1954). Accepting only stems of *dbh* > 0.01 m, no departure from random spacing could be detected. Tree heights, Fig. 1, were determined on the study plots by triangulation. Whitfield *et al.* (1977) and J. M. Mayo (personal communication) made detailed geometric measurements on a sample of 10 trees, from which the element size and orientation distributions used in Eq. 8 were derived, as well as the element vertical distributions of Fig. 1, canopy radius as a function of tree height, and tree top cone apex half angle, α_t (=12°).

Optical properties of the elements

The needled shoot opaque fraction, $\Omega(\alpha)$, used in Eq. 8, was measured from photographs of shoots. These were overlaid with masks representing $A(\alpha)$, the shoot outline projected area, and analyzed in a densitometer. The results appear as points in Fig. 3, together with a quadratic curve used for calculations.

The scattering submodel requires as parameters the reflectivity, transmissivity, and absorptivity of the scattering elements and of the ground surface. Only needles have nonzero transmissivity. We measured needle properties with an integrating sphere, using the substitution method described by Birkebak and Birkebak (1964). The detector was an ISCO model SR spectroradiometer connected to the sphere by a bundle of optical fibres. The sample was a set of needles laid so closely together as to allow no detectable spaces.

The reflectivities of other elements are much less critical in determining the behaviour of scattered radiation and we were content to accept estimates from the literature (e.g., Norman and Jarvis 1975). Table 2 summarizes the optical properties of all elements.

TABLE 2. Optical properties of the elements

	Visible[a]		Infrared[b]	
Element type	τ	ρ	τ	ρ
Needle	0.03	0.28	0.25	0.45
Trunk	0	0.05	0	0.05
Cone	0	0.1	0	0.1
Live branch	0	0.05	0	0.05
Dead branch	0	0.05	0	0.05
Ground surface	0	0.2	0	0.2

[a]Average over the wavelength range 400–700 nm.
[b]At 780 nm.

Results from the model and comparison with measurements

Representative results from the penetration part of the model are shown in Fig. 4. Figure 4*a* compares the effects of the various intercepting elements and illustrates the variation of P^n with η. The first and most important thing to note from this figure is the dominant role of needle clumps compared with other elements. Also apparent are the almost total lack of interception in the top metre of the canopy and the effects of element height distributions (Fig. 1); cones have their influence near the top of the canopy, dead branches near the bottom. In Fig. 4*b*, the overall impact of all elements is illustrated. Note the effect of slope angle, in that for $\eta = 20°$, rays from $\phi = 0°$ are much more attenuated than from $\phi = 180°$; this is reduced for greater values of η. Also shown in this figure is the integrated attenuation from a uniformly luminous sky ($\bar{P}$).

The other two geometries considered, a horizontally random canopy and flat-topped trees, differ from the above only in the horizontal distribution of elements. Pertinent output from these calculations is illustrated in Fig. 5. Comparison with the corresponding curves of Fig. 4*b* reveals considerable differences, mainly in the degree of attenuation in the upper canopy. The two clumped models show the same rate of attenuation deep in the canopy, as expected.

The behaviour of scattered radiation for some typical cases is revealed in Fig. 6. The difference between the scatter of visible and near-infrared radiation is the result of needle optical characteristics.

As described above, our measurements of radiation interception were made by moving sensors horizontally through the forest canopy; each transect required about 10 min, and between transects the sled had to be hauled back and repositioned and a side-by-side comparison made with output from the tower-top sensors. Consequently solar position changed during the course of one set of measurements, and in making computations to compare with the data, the model had to be run separately for times when the instruments were at the centre point of each transect. In Fig. 7 we superimpose one set of meausrements on the output of the three models.

Rather than repeat this sort of presentation for each of the data sets, we compare predicted and measured values for the three models (Fig. 8). We distinguish those points taken in the morning from those of the afternoon. The main result is that our primary model accounts reasonably well for afternoon measurements, while the morning ones appear to fit between the flat-topped and random models. This conclusion will be explored in the next section.

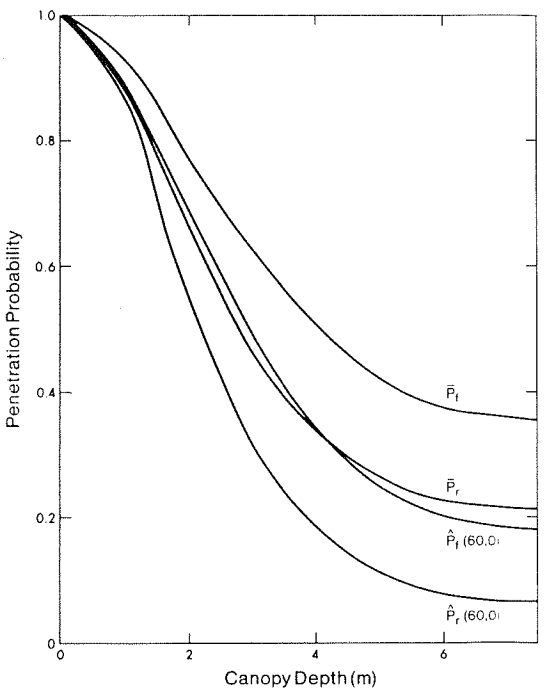

FIG. 5. Penetration probabilities for the random model ($\hat{P}_r$ and $\bar{P}_r$) and flat-topped tree model ($\hat{P}_f$ and $\bar{P}_f$).

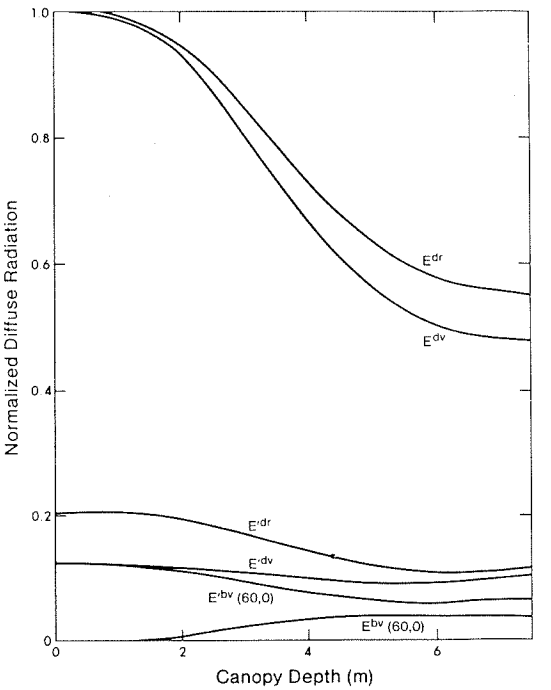

FIG. 6. Some results from the scattering model. Superscripts d and b refer to radiation originating as sky diffuse and solar beam, respectively, superscripts r and v refer to near infrared and visible radiation, respectively, and the unprimed and primed quantities are downward and upward fluxes, respectively.

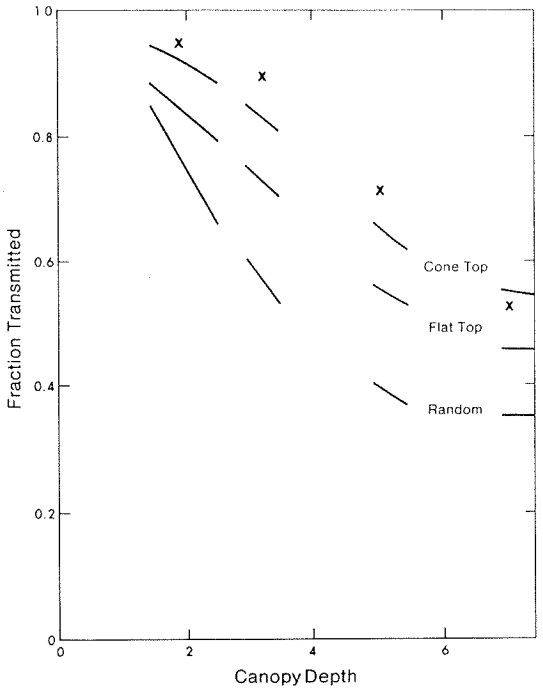

FIG. 7. The comparison of one set of measurements with predictions of the three models. The × marks are average values of visible radiation penetration along 20-m horizontal transects, given as ratios to radiation incident above the canopy.

Also indicated in Fig. 8 are the results of measurements of diffuse radiation attenuation, made in early morning with the sun behind the hill. Note that the random model best accounts for these results.

Discussion and conclusions

Our main model is free of tuning parameters: there are no unknown or empirical parameters which are to be adjusted to produce a good fit to the data. One could feel free to vary a few parameters which are subject to measurement uncertainty, but no reasonable adjustment would modify the results as much as going to the flat-topped or random model. These really are new models, which have built into them considerably different assumptions of gross canopy geometry. Thus, the observation of good fit to the main model for afternoon measurements and not for morning ones should be explained in terms of canopy geometry. In fact, there is an aspect of this geometry which has not yet been accounted for, and that is the azimuthal asymmetry of element location, indicated in Fig. 9. This shows a pronounced aggregation of needle clumps into the southwest quadrant with respect to the tree trunk. Also indicated on this figure are the slope azimuth projection of a normal to the slope onto the horizontal, measured from true north, and the ranges of sun azimuth for the morning and afternoon measurements. It is apparent that the tree shape, seen from the sun direction, is very different from the two sets of measurements. We

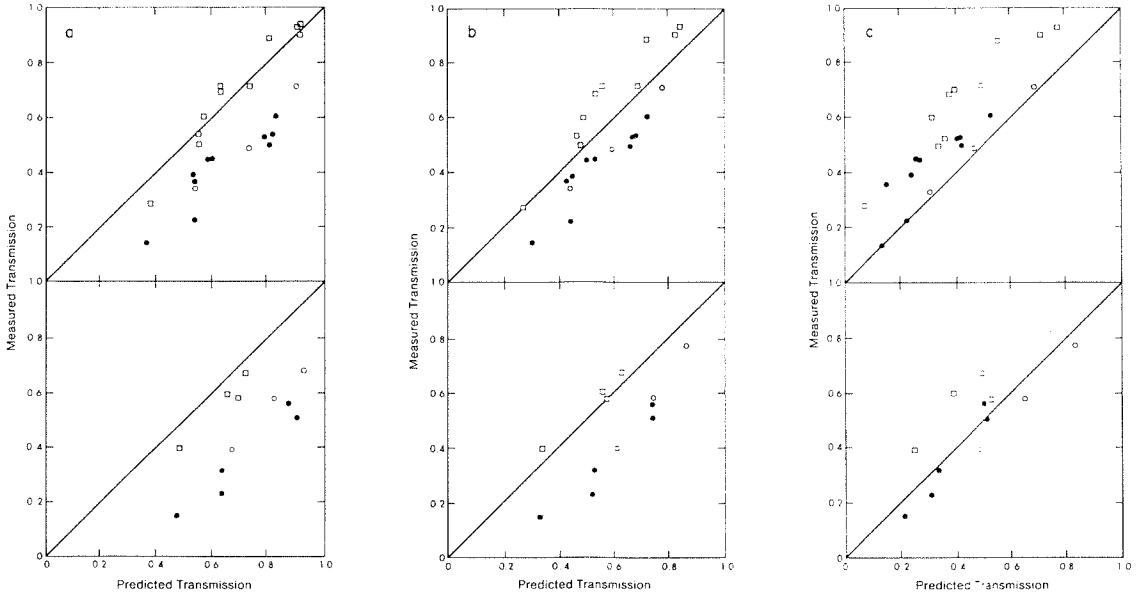

FIG. 8. Comparisons of radiation attenuation measurements to predictions of the three models. In each case the upper panel refers to visible light (400–700 nm) and the lower panel refers to near infrared (780 nm). The open squares designate afternoon readings, the solid circles designate morning ones, and the open circles designate readings of diffuse radiation made with the sun below the hill limb. (*a*) Cone-topped tree model (*b*) flat-topped tree model; (*c*) random element distribution model.

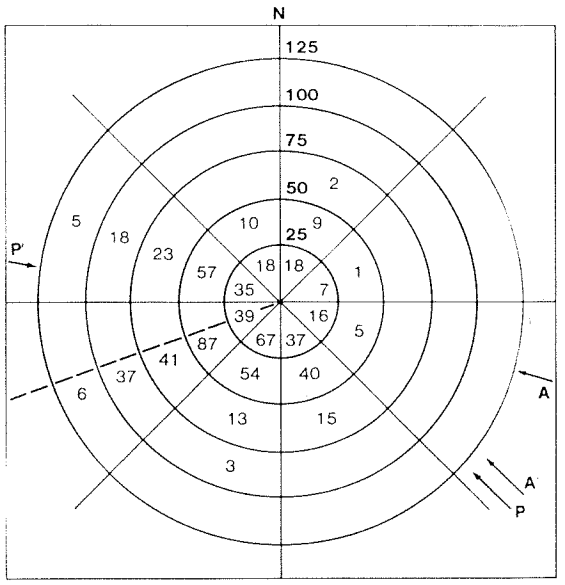

FIG. 9. The numbers of needled shoots in various radial and azimuthal positions with respect to the trunk for an intensively harvested tree (Whitfield *et al.* 1977). The arrows labelled *A* and *A'* delimit the sun azimuth for morning measurements, and P and P' delimit the sun azimuth for afternoon ones. The broken line indicates hill azimuth direction. The circle radii are given in centrimetres.

suggest that it is as a consequence of such asymmetry that we find the ability of the models to fit the data varying through the day. A test of this conjecture would require construction of a new model with asymmetrical trees.

That the random model best accounts for the diffuse attenuation measurements is probably the result of the discrepancy between our assumption of a uniformly luminous sky and the real situation in which a preponderance of the sky radiation comes from near the direction of the sun (Kondratyev 1969), which in this case would be from near the horizon of the hillside system.

Note that our treatment of needled shoot gaps in Eq. 8 is equivalent to Norman and Jarvis's (1975) handling of shoot gaps and whorl gaps. They take the 0th, 1st, ... *i*th terms of a Poisson distribution series as representing the probability of altogether missing an element, passing through a gap in one but missing others, ... passing through gaps in *i* elements but missing others. However, when their series is summed, it reduces to simple exponential attenuation by elements having the area of the element projected outlined multiplied by the opaque fraction.

A reviewer pointed out that we failed to account for multiple transmissions and reflections within needle clumps in our treatment of scattered radiation. This could affect the model outcome, particularly in the near infrared, for which the transmission and reflection coefficients of needles are relatively large. Adequate treatment of this problem would constitute a significant achievement in itself. A very rough idea of the consequence of multiple, straight-line transmissions may be obtained as follows. Data of ours, not presented here, show that the ratio of projected needled shoot area to needle surface area is about 0.15. The needles have half-circle shapes in cross section, and the projected surface area of a cylinder of that shape, averaged over all viewing directions, for a length-to-radius ratio of 40, is 0.204 of actual surface area; thus, $0.15/0.204 = 0.75$ of projected needle area is not overlapping or overlapped by other needle projections. Assuming, crudely, that the needles in a clump are randomly placed and oriented, this is the zero term of a Poisson distribution, of which the next three terms (representing single, double, and triple overlaps) are 0.22, 0.03, and 0.003). From Table 2, transmissivity of a needle at 780 nm is 0.25, so that total transmission through needles (not through the gaps between needle projections) is $0.75 \times 0.25 + 0.22 \times 0.25^2 + 0.03 \times 0.25^3 + \ldots = 0.202$, or 80% of single needle transmission. Shoot reflectance may be closer to needle reflectance than this. In any case, it could be that a proper treatment of these effects might make the visible and near-infrared results, expressed in Fig. 8, more similar.

The same reviewer pointed out that our measured needle reflectance in the visible, 0.28, is rather large when compared with values in the literature. The reason for this is unknown but may be related to the specular nature of reflection from these needles at large incidence angles.

The basic methodology presented here is readily adaptable to all sorts of tree shapes. Essentially any radially symmetric shape can be put together by combining spheres, ellipsoids, cylinders, and cones, and the interception of any of these shapes with straight lines is described by quadratic equations. Situations in which leaves are confined to a shell around the outside of a tree shape can be handled by considering one envelope inside another and taking the ray path only between envelopes.

Acknowledgements

We wish to thank George Reynolds, Janet Marsh, and George Davis for invaluable assistance with the field measurements and Paul McCourt and Arun Jumar for programming. Murray Hunt constructed and operated the integrating sphere. Cheryl Bradley measured the tree heights and stem densities. Funding was provided by the Alberta Oil Sands Environmental Research Program and the National Research Council of Canada.

ALLEN, L. H., JR. 1974. Model of light penetration into a wide-row crop. Agron. J. **66**: 41–47.

BIRKEBAK, R., and R. BIRKEBAK. 1964. Solar radiation characteristics of tree leaves. Ecology, **45**: 646–649.

BROWN, P. S., and J. P. PANDOLFO. 1969. An equivalent-obstacle model for the computation of radiative flux in obstructed layers. Agric. Meteorol. **6**: 407–421.

CARROLL, S. B., and L. C. BLISS. 1982. Jack pine – lichen woodland on sandy soils in northern Saskatchewan and northeastern Alberta. Can. J. Bot. **60**. In press.

CHARLES-EDWARDS, D. A., and J. H. M. THORNLEY. 1973. Light interception by an isolated plant — a simple model. Ann. Bot. (London), **37**: 919–928.

CLARK, P. J., and F. C. EVANS. 1954. Distance to nearest neighbor as a measure of spatial relationships in populations. Ecology, **35**: 445–453.

KONDRATYEV, K. YA. 1969. Radiation in the atmosphere. Academic Press, New York.

MANN, J. E., G. L. CURRY, D. J. HARTFIEL, and D. W. DEMICHELE. 1977. A general law for direct sunlight penetration. Math. Biosci. **34**: 63–78.

MANN, J. E., G. L. CURRY, and P. J. H. SHARPE. 1979. Light interception by isolated plants. Agric. Meteorol. **20**: 205–214.

MONSI, M., and T. SAEKI. 1953. Über den Lichtfaktor in den Pflanzengesellschaften und seine Bedeutung fur die Stoffproduktion. Jpn. J. Bot. **14**: 22–52.

MONSI, M., Z. UCHIJIMA, and T. OIKAWA. 1973. Structure of foliage canopies and photosynthesis. *In* Annual reviews in ecology and systematics. *Edited by* R. F. Johnston. Annual Reviews Inc., Palo Alto, CA.

NILSON, T. 1971. A theoretical analysis of the frequency of gaps in plant stands. Agric. Meteorol. **8**: 25–38.

NORMAN, J. M. 1975. Radiative transfer in vegetation. *In* Heat and mass transfer in the biosphere. I. Transfer processes in plant environment. *Edited by* D. A. deVries and N. H. Afgan. Scripto Book Co., Washington. pp. 187–206.

NORMAN, J. M., and P. G. JARVIS. 1974. Photosynthesis in sitka spruce. III. Measurements of canopy structure and interception of radiation. J. Appl. Ecol. **11**: 375–398.

——— 1975. Photosynthesis in sitka spruce. V. Radiation penetration theory and a test case. J. Appl. Ecol. **12**: 839–878.

OIKAWA, T., and T. SAEKI. 1972. Light regime in relation to population structure — an experimental approach based on the Monte-Carlo simulation model. Rep. 1971 IIBP/PP Photosynthesis Level III Group, Tokyo. pp. 197–216.

ROSS, J. 1975. Radiative transfer in plant communities. *In* Vegetation and the atmosphere. Vol. 1. Principles. *Edited by* J. L. Monteith. Academic Press, London, New York, and San Francisco.

ROWE, J. S. 1972. Forest regions of Canada. Information Canada, Ottawa.

TANAKA, S. 1968. Estimation of sunlit leaf area in tobacco community by Monte-Carlo method. (*1*) Estimation on direct sunlight of a plant. Environ. Control Biol. **7**: 12–16. (In Japanese.)

WHITFIELD, D. W. A., J. M. MAYO, J. E. HARTER, S. NELSON, and A. MEHLENBACHER. 1977. Tree geometry and optical properties of leaves. *In* Long term prediction of vegetation performance on mined sands. *Edited by* L. C. Bliss. Report of the Alberta Oil Sands Environmental Research Project, VE 6, Government of Alberta.